

Active-Site Dynamics and Large-Scale Domain Motions of Sulfite Oxidase: A Molecular Dynamics Study

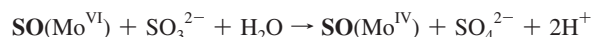
M. Jake Pushie and Graham N. George*

Molecular and Environmental Science Research Group, Department of Geological Sciences, University of Saskatchewan, 114 Science Place, Saskatoon, Saskatchewan, S7N 5E2, Canada

Received: September 9, 2009; Revised Manuscript Received: December 21, 2009

The physiologically vital enzyme sulfite oxidase employs rapid intramolecular electron transfer between a molybdenum ion in the C-terminal domain (the site of sulfite oxidation) and a heme moiety in the N-terminal domain to complete its catalytic cycle. Crystal structures of the enzyme show C- and N-terminal domain orientations that are not consistent with rapid intramolecular electron transfer. Domain motion has been postulated to explain this discrepancy. In the present work we employ molecular dynamics simulations to understand the large-scale domain motions of the enzyme. We observe motion of the N-terminal domain into an orientation similar to that postulated for rapid electron transfer. Our simulations also probe the dynamics of the active site and surrounding residues, adding a further level of structural and thermodynamic detail in understanding sulfite oxidase function.

The trace element molybdenum is selectively utilized in biological systems and is critical for the functioning of an ancient family of oxotransferase enzymes found in almost all prokaryotic and eukaryotic organisms. Sulfite oxidase (SO) is the prototypical member of a major family of molybdenum enzymes (called the sulfite oxidase family) and is representative of the Mo-based oxo-transferases in general. It catalyzes the oxidation of sulfite to sulfate:¹



With the exception of nitrogenase,² all molybdenum enzymes that have been described to contain a novel pyranopterin–dithiolene cofactor (known as molybdopterin) in which the Mo atom is coordinated by the dithiolene moiety.^{3,4} In sulfite oxidase, the Mo atom is coordinated by two sulfur donors from one dithiolene, two terminal oxygen atoms, and one additional sulfur donor from a cysteine (Cys185 in chicken SO, or Cys207 in human SO).

The importance of SO is underscored by its ubiquitous presence in almost all organisms; for example, SO is located in the inner-membrane space of mitochondria of eukaryotic cells and is also found in green plants⁵ and in certain bacteria.⁶ A number of clinical mutants of SO have been identified which are associated with very severe neurological impairment and early death in humans,⁷ and a mutation in the untranslated 5'-region of the SOX gene, together with exposure to the molybdenum antagonist tungsten, has been implicated in a Nevada leukemia cluster.⁸

SO exists as a homodimeric protein, shown in Figure 1A, with a subunit mass of approximately 55 kDa. Each subunit consists of two domains: a large C-terminal domain which contains the active site (Figure 1C) and a smaller N-terminal domain which contains a cytochrome *b*₅-type heme prosthetic group (Figure 1D). The active site is accessible by a channel

within the C-terminal domain. During enzymatic turnover, the active site cycles from a dioxo-Mo^{VI} form, its resting state, to a reduced oxo-Mo^{IV} form before being reoxidized back to Mo^{VI} through a series of intramolecular electron transfer (IET) reactions to the cytochrome *b* site in the N-terminal domain (a process which proceeds via an intermediate Mo^V form) and which ultimately transfers electrons to an external electron acceptor, ferricytochrome *c*.

Many molybdenum enzymes contain more than one redox active center, with IET between the molybdenum and the other redox active center being essential for completing the catalytic cycle. The crystal structures of many of these enzymes are now available,^{9–11} and in almost all instances the pterin appears to lie between the molybdenum and other redox active site, strongly suggesting a role for the pterin heterocycle in facilitating IET. The sole exception to this is sulfite oxidase, where the pterin points away from the heme in a position which would be highly unfavorable for the pterin to act in facilitating IET (shown in detail in Figure 1B).

The N-terminal domain of SO has been proposed to interact with the opening of the channel leading to the active site in the C-terminal domain¹² as this close association would facilitate IET during catalytic turnover. Kawatsu and Beratan have also analyzed IET between enzyme domains joined by a flexible tether and found that there is a significant entropic component to the donor–acceptor potential governed by the flexibility of the tether.¹³ In the absence of the electron-accepting N-terminal heme domain the C-terminal domain maintains its dimeric structure and is catalytically active in the presence of terminal electron acceptors, such as ferricyanide.¹⁴

Within the active site, R138 (chicken SO numbering) has been proposed to be important for substrate specificity and mutation of this conserved residue in human SO (R160Q) can be lethal¹⁵ and has been shown to structurally perturb the molybdenum site.¹⁶ Additionally, Y322 (Y343 in human SO) is also involved in substrate recognition and catalytic activity^{17–20} and is situated adjacent both the active site and R138 and interacts directly with a bound sulfate in the 1SOX crystal structure.⁹

* Author to whom correspondence should be addressed. E-mail: g.george@usask.ca. Tel.: +1-306-966-5722. Fax: +1-306-966-8593.

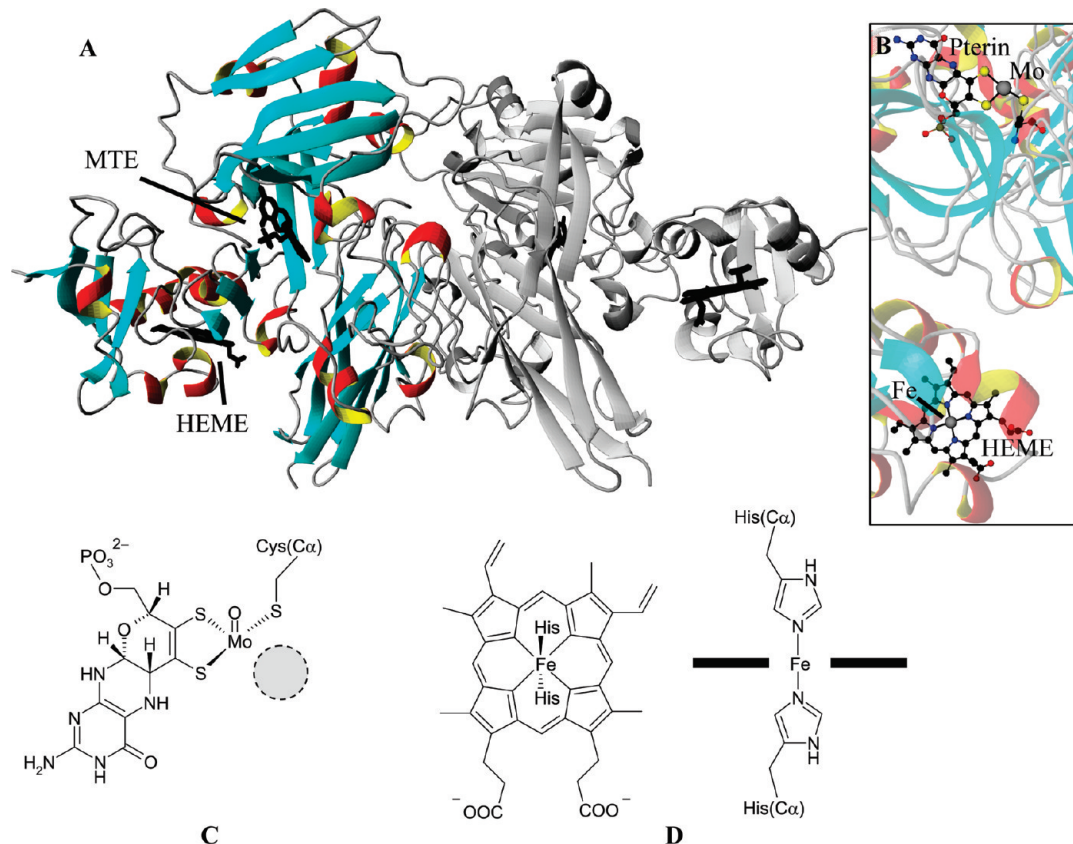


Figure 1. (A) 1SOX crystal structure with the domain used in simulations highlighted for clarity. Structures of the prosthetic groups (heme and molybdopterin, abbreviated HEME and MTE, respectively) are shown. (B) Reoriented view of the separation between the MTE and HEME sites from the 1SOX crystal structure, showing the orientation and direction of the pterin cofactor. (C) Scheme of the coordination environment in the Mo-containing active site, with the vacant coordination site at the Mo atom highlighted. (D) Scheme of the coordination environment of the Fe-containing heme site, shown top-down and edge-on.

In this initial study our aim was to examine the dynamic motion of the N-terminal and C-terminal domains as well as dynamics of the active site, in the absence of substrate or product, for the purposes of establishing a starting reference for future simulations. The model chosen represents a fully reduced form for both the molybdenum active site (Mo^{IV}) and the cytochrome b_5 type heme (Fe^{II}). The Mo^{IV} form is initially formed upon product formation before being reoxidized to Mo^{VI} , via a Mo^{V} intermediate. The Fe^{II} -containing heme prosthetic group was parametrized for simplicity and to maintain its structural integrity as well as that of the N-terminal heme domain in this initial study. The model affords a means of studying the mobility of the heme-containing N-terminal domain, which is responsible for shuttling electrons from the active site to an external electron acceptor. The dynamic motion of the active site and surrounding residues adds a further level of structural and thermodynamic detail to understand SO function. Simulation results are compared and contrasted with the 1SOX crystal structure of SO and demonstrate the feasibility of future large-scale simulations of molybdo-enzymes.

Methods

Setup of Sulfite Oxidase Structure. The initial structure used in all simulations was generated from the chicken sulfite oxidase (cSO) crystal structure, 1SOX.⁹ The cSO dimer, containing over 14 000 atoms, is a relatively large protein for structure dynamics calculations in explicit solvent. Because computational overhead for such calculations scales maximally with the square of the number of atoms, half of the dimer was modeled in this initial

study to reduce computation time. The half of the dimer is shown emphasized relative to the full cSO dimer in Figure 1A (we note that this did not require breakage of any disulfide linkages or other chemical bonds). Missing atoms in the disordered region that links the heme-containing N-domain and the active site-containing C-domain were not resolved crystallographically⁹ and were added manually to the dangling bonds. The added atoms (residue Ala89 and the side chains of Asp85 and Glu86) were generated so that they maintained allowable ϕ , ψ , and χ angles. The protonation state of each His residue in the protein was assigned manually, based on the most favorable local environment for H-bonding and charge in the 1SOX crystal structure. His residues 40 and 65 were protonated only at the N δ 1 position as the N ϵ 2 atoms coordinate to the iron center of the heme.

Density Functional Calculations. Closed-shell Mo^{IV} and Fe^{II} hybrid density functional calculations, using the Becke-3-LYP hybrid functional method,²¹ were carried out using the Gaussian 03 (Revision E.01) suite of software.²² Geometry optimizations on model structures of the Fe^{II} heme and Mo^{IV} active-site environments were performed without geometry or symmetry constraints using a mixed basis set approach, consisting of the LANL2DZ effective core potential basis set for each of the metal atoms, and 6-31G(d) for the remaining atoms. Optimized structures are shown in the Supporting Information Figure S1 and the related structures of the Mo-containing active site and Fe-containing heme are represented in Figure 1, C and D, respectively. Structures were considered optimized when the

change in energy between subsequent optimization steps fell below 0.03 kJ mol^{-1} .

Harmonic frequencies of the optimized structures were calculated to verify each was at a stationary point on the potential energy surface (no imaginary frequencies) and also to provide force constants for force field models of each structure. Force constants for the Mo–ligand bonds to be represented in the force field for simulations were taken from harmonic frequency output and scaled by 60230 to convert Gaussian03 force constants in mdyn/\AA into kJ/mol/nm^2 for the OPLS-AA/L force field.^{23,24}

Unique and Modified Residue Topologies. Mo^{IV} –Pterin. Equilibrium Mo^{IV} –ligand bond lengths, derived from extended X-ray absorption fine structure (EXAFS) data were as follows: Mo^{IV} –S(dithio) = 2.42 \AA , Mo^{IV} –S(Cys) = 2.42 \AA , Mo^{IV} = O(oxo) = 1.72 \AA .^{25,26} The remaining equatorial coordination site indicated in Figure 1C, normally occupied by a water molecule (or possibly OH^-), was not explicitly defined to allow dynamic exchange of solvent molecules during simulations. Additional parameters for the Mo^{IV} -containing system, such as angles and dihedrals, were derived from models optimized at the B3LYP/LANL2DZ:6-31G(d) level using Gaussian03 (described above). Mo^{IV} –ligand force constants were taken from harmonic frequency calculations, and atomic charges generated using the CHelpG method²⁷ – both calculated at the same level of theory as structure optimizations, following previously published methods.^{28,29} The DFT-optimized structure is shown in Figure S1A of the Supporting Information. The overall charge for the force field representation of the Mo^{IV} (=O)(pterin) moiety is -2.6 , which is designed to be combined with the deprotonated Cys185 residue for a total charge of -3 (note that the pterin includes the R-OPO_3^{2-} group).

Deprotonated Cysteine Residue. Charges for the deprotonated Cys residue (bound to the Mo^{IV} center in Figure 1C) topology were taken from the Mo^{IV} DFT model, with the charges on the backbone atoms maintained from the parent OPLS-AA/L Cys topology.^{23,24} The total charge of the deprotonated Cys residue is -0.400 (as opposed to -1), with the S^- atom bearing a -0.620 charge, which reflects its charge delocalization when coordinated to the Mo^{IV} center.

Rigid b_5 -Type Heme. As we were not specifically simulating the dynamics of the heme moiety in this initial study, fixed force constants for bonds within the heme were used (implemented force constants were approximately midway between that of a $\text{C sp}^3\text{--C sp}^3$ and a $\text{C sp}^2\text{--C sp}^2$ bond, $250\,000 \text{ kJ/mol/nm}^2$), to ensure that the heme maintained its overall structure. His40 and 65 are involved in coordination to the Fe^{II} center of the heme moiety and are therefore explicitly bound to the Fe^{II} atom in simulations. The Fe^{II} –ligand bond lengths were taken from a DFT model of Fe^{II} (porphine-_{2H})(4-methylimidazole)₂, shown in the Supporting Information, Figure S1B, with Fe^{II} –N(porphine) = 2.02 \AA and Fe^{II} –N ϵ 2(His) = 2.01 \AA . We note in passing that gas-phase geometry optimization of the full Fe^{II} (porphyrin-_{2H})(4-methylimidazole)₂ structure is problematic and often results in significant distortions in the Fe^{II} ligand sphere as the anionic carboxylate groups tend to form strong H-bond interactions with the N(H) sites of the apical imidazole ligands. CHelpG charges were also generated from the Fe^{II} (porphine-_{2H})(4-methylimidazole)₂, while charges for the porphyrin ring substituents, such as the alkene and carboxylic acid groups, utilized charges from groups already present in the OPLS-AA/L force field.^{23,24}

Additional Parametrization. In addition to the ligand–metal bonds, angles and improper dihedral angle constraints and the

list of 1–4 pair interactions for each of the His- Fe^{II} -heme and Cys185- Mo^{IV} -pterin prosthetic groups were added to the molecular topology. The OPLS-AA/L force field was also updated with the average mass for molybdenum, 95.94 mu , as well as Lennard-Jones parameters for molybdenum: $\sigma = 0.2694 \text{ nm}$, $\epsilon = 0.845\,17 \text{ kJ mol}^{-1}$.³⁰ Parameters for iron were already present in the OPLS force field.^{23,24}

Molecular Dynamics Simulations. MD simulations were carried out using GROMACS, version 3.3.3.^{31,32} The all-atom OPLS-AA/L force field^{23,24} was employed for simulations, supplemented by parameters for the Mo and Fe coordinating environments, detailed above. The temperature was kept constant (300 K , $\tau_T = 0.1 \text{ ps}$) by weakly coupling the system to an external temperature bath.³³ Interactions were updated iteratively using a grid-based neighbor search algorithm and was updated every 10 steps with a neighbor list of 1 nm . Pressure was maintained at 1 bar with isotropic temperature coupling ($\tau_P = 1.0 \text{ ps}$) and compressibility of $4.5 \times 10^{-5} \text{ bar}^{-1}$. The particle-mesh Ewald (PME) method was employed for long-range electrostatics, with a cutoff of 1 nm .³⁴ The linear constraint solver (LINCS) was used to constrain bond lengths within the protein and prosthetic groups.³⁵ van der Waals interactions were calculated using a twin-range cutoff, both set to 1 nm . Simple point charge (SPC) waters^{33,36} were used in all simulations and were constrained using SETTLE.³⁷

In order to make these simulations more computationally tractable, we elected to employ a longer time step for each iteration in order to reach longer durations. The most direct way this can be achieved is to slow the fastest motions within the simulation, i.e., R–H bond vibrations. To this end, the mass of all hydrogen atoms was increased to 4.032 mu and the increased mass was concomitantly subtracted from their parent heavy atoms to maintain the same total mass of the system. Within the protein this effectively reduces the vibrational frequency of C/O/N–H bonds and slows dihedral motions. With such changes, a longer 5 fs time step was implemented, as has been successfully demonstrated previously.^{38–40} This time step was chosen as a small but reasonable increase above the more commonly implemented 2 fs time step used in GROMACS simulations. Inappropriately long time steps can cause energy instabilities in the simulations leading to heating due to force errors,⁴¹ which would be reflected in the results. We therefore monitored the temperature and λ (a measure of heat flow between the simulation and the external bath) for each simulation. Temperatures averaged from all simulation data were 299.641 ± 0.002 with an rmsd of 0.864 ± 0.015 and a total drift (over the entire simulation times) was -0.017 ± 0.104 , while λ for the protein and nonprotein systems averaged to 1 in all cases, indicating no significant heating or cooling effect from the external bath.

The half-dimer was simulated in a square box, 83 \AA per side, with periodic boundary conditions. The box was filled with 16286 SPC water molecules and 10 Na^+ counterions, for a total system charge of zero. The system was energy minimized and then eight simulations were separately equilibrated for 10 ns prior to production runs (protein root mean square deviations stabilized in all simulations by $\sim 10 \text{ ns}$). Each of the eight simulations were run uncoupled to one another, in parallel, for approximately $30\text{--}45 \text{ ns}$ each (total simulation time = $\sim 240 \text{ ns}$).

Elastic Network Model Normal-Mode Analysis. To identify large-scale domain motions between the N-terminal and C-terminal domains normal-mode analysis was performed using the online tool: normal-mode analysis, deformation, and refine-

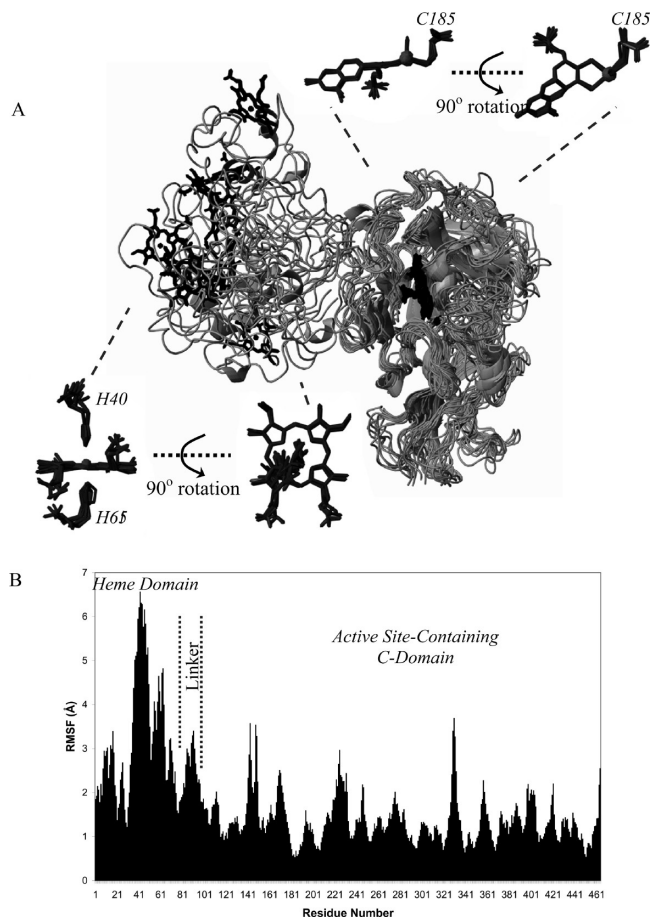


Figure 2. Overlay of 10 randomly selected structures from the simulations, rms-fitted using the C-domain heavy atoms, highlighting the dynamic motion of the heme domain relative to the active-site-containing C-domain. The prosthetic groups and protein-anchoring residues are shown separately in different orientations. The root-mean-square fluctuation (RMSF) for the protein Cα atoms is shown, generated from aggregated data from all simulations (~256 ns).

ment (NOMAD-REF).^{42–44} Using the heavy atoms from representative conformations generated during the dynamics simulations, an elastic network normal-mode analysis was performed using the default settings of the server. Interactions within the elastic network model used an elastic network atom pair cutoff of 10 Å in the mode calculations to define which pairs were linked by a spring force constant using a distance–weight parameter of 5 Å to provide a smoother cutoff for pair interactions.

Results

Stabilities of the Heme-Containing and Active-Site-Containing Domains. Figure 2A shows an overlay of the C-terminal domain for 10 randomly selected structures from the simulations and demonstrates the mobility of the heme-containing N-terminal domain relative to the C-terminal domain. Figure 2A also shows overlays of the Fe^{II} heme and Mo^{IV} pterin groups, demonstrating their structural stability. The root mean square fluctuation (RMSF, shown in Figure 2B) gives a measure of the standard deviation of the protein backbone Cα-atom positions over several simulations. As expected, residues with high RMSF values correlate with surface-exposed regions and loops (particularly those in the heme-containing N-terminal domain) while residues with low RMSF values most often correspond to buried residues within the protein. The linker

region between the two domains (indicated in Figure 2B) also demonstrates increased conformational flexibility.

Root mean square deviation (rmsd) analyses (not illustrated) of the N-terminal and C-terminal domains separately show that each is stable following the equilibration phase in each simulation and remain stable during the course of simulations.

Domain Motions and Normal-Mode Analysis. In the 1SOX crystal structure the Fe and Mo atoms within each monomer are separated by ~32 Å, with a domain orientation that appears unfavorable for IET. The closest approach observed in our simulations was 27.4 Å and the largest separation was 56.9 Å, where the heme domain is fully extended into solution. Normal-mode analysis was performed on representative conformations from the simulations, representing the fully extended heme-containing N-terminal domain (Figure 3A), as well as a conformation where the protein is more compact than the crystal structure (Figure 3B). Analysis reveals that the linker connecting the N-terminal and C-terminal domains (which was disordered in the crystal structure, leading to poorly resolved residues) can act as a hinge, likely facilitating close association of the heme-containing N-domain with the C-domain for intermolecular electron transfer. The flexible linker also allows the heme domain to extend out from the enzyme into solution, thereby facilitating intramolecular electron transfer. Motions of the two domains include wagging of the N-terminal domain as well as twisting and rotations (see Figure S2 in the Supporting Information for representative structures).

Dynamics of the Molybdenum-Containing Active-Site Residues. The active-site residues R138 and Y322 are known to be catalytically important for substrate specificity and enzyme function. We observe that these residues, particularly Y322, can serve to partition the active-site environment for extended periods in the simulations. The Y322 hydroxyl moiety is an average of 5.6 ± 0.3 Å from the Mo^{IV} center, measured from the Cζ atom (the para position carbon, shown in Figure 4A). The Tyr side chain is also observed to transiently move out to 10.1 ± 0.9 Å during simulations, and in two simulations the hydroxyl O atom briefly interacts directly with the equatorial coordination site at the Mo^{IV} center following dissociation of the equatorial water molecule. This latter interaction may be an artifact of the labile nature of the primary coordination sphere water molecules due to the force field representation and is only accessed in two simulations (combined time is ~20 ns out of the ~240 ns simulation time). The Y322 hydroxyl also H-bonds with the closest of the pterin dithiolene ligands in several simulations for extended durations, typically for 5–10 ns.

The active-site residue Y322 exhibits a relatively large range of motion in the simulations and effectively screens all molecules entering or exiting the active site, a role which has been proposed by Pacheco et al.¹⁹ To a lesser extent R450 and R138 also interact with solvent in the active-site channel. Over its dynamic range of motion Y322 occupies two major positions in the active-site channel. Figure 5 shows the two primary orientations of Y322 in the active-site channel. Panels A and B in Figure 5 show the same orientation of Y322 in two different cutaway depths to better highlight the channel of water molecules below the Tyr side chain. In Figure 5A, the Tyr side chain occupies a position in the foreground, on one side of the channel, close to R138 and the pterin cofactor. Alternatively, the side chain may also occupy a position approximately 90° from its position in panel A, where the Tyr residue resides along a different “face” of the active-site channel, further from R138 and the pterin, shown in Figure 5C.

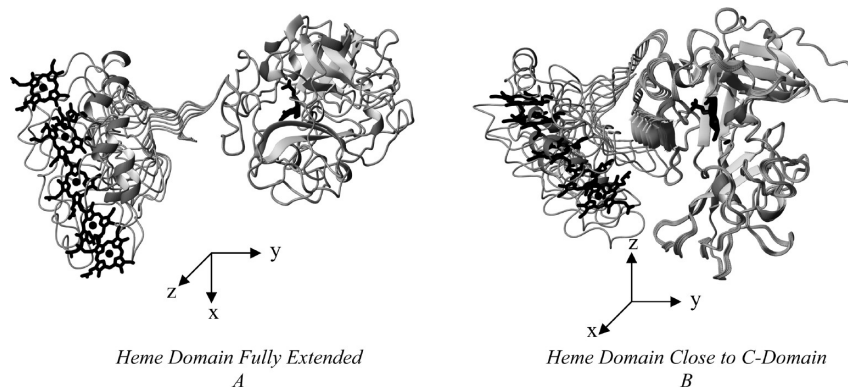


Figure 3. Representative normal-mode analysis (NOMAD-ref structures) for an extended and close-associating heme domain showing principal modes of motion.

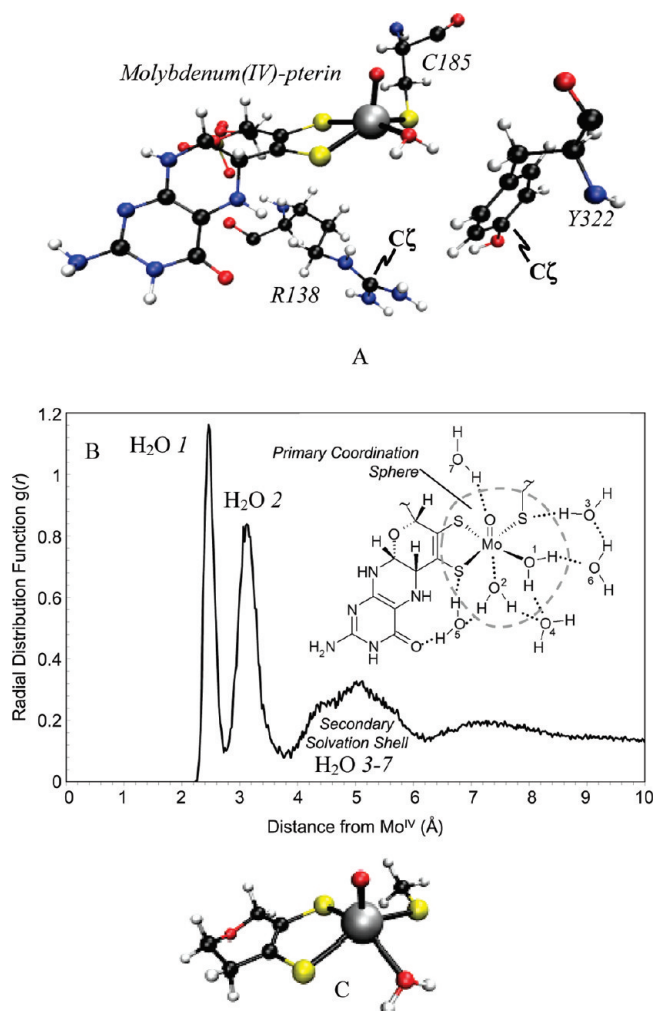


Figure 4. (A) Representative snapshot of the Mo^{IV} active site with an equatorially bound solvent molecule explicitly shown as well as representative orientations of R138 and Y322. (B) Radial distribution function for molybdenum and solvent. Shown inset is a schematic representation of the variably occupied waters within the active site. Presence of H_2O 1 (equatorial position) is highly populated and seldom exchanges. H_2O 2 (axial position) is highly populated but exchanges frequently, while the remaining water positions in the secondary solvation shell (denoted as H_2O 3–7) are less frequently occupied and exchange readily. (C) DFT-optimized structure of the equatorially bound water molecule at the Mo^{IV} active site.

The separation between R138 and the Mo^{IV} center ranges from 5 to 8 Å, measured between the Mo atom and the $\text{C}\zeta$ atom of the Arg side chain (shown in Figure 4A). In all

simulations, R138 maintains its proximal position within the active site and does not appear to undergo significant conformational changes or displacement. No other significant conformational or structure changes are observed for other residues in the vicinity of the active site in these simulations. Two residues, R450 and D321, located along the entrance to the active-site channel, interact with one another primarily via a salt bridge that resides on the opposite face of Y322 from the Mo^{IV} active site and this interaction persists in all simulations. Occasionally, this interaction is disrupted, allowing R450 to interact with solvent molecules entering or exiting the active-site channel. In the ISOX crystal structure, R450 is observed to interact with a sulfate molecule in the active-site channel, very close to the active site.

Two other ligands, the backbone amide protons of A186 and A297, H-bond directly to the apical oxo moiety in the Mo^{IV} active site during simulations. In the crystal structure, the backbone of A186 and A297 are 3.0 and 3.1 Å from the oxo ligand, respectively. The A186 residue maintains a H-bonding distance of 1.98 ± 0.23 Å between the Ala N(H) and the active site $\text{O}=\text{Mo}$ during all simulations. A297, on the other hand, forms a more facile H-bond, with an average length of 2.19 ± 0.37 Å, which breaks frequently, where the $\text{A297 N(H)}-\text{O}=\text{Mo}$ separation increases to 3.65 ± 0.22 Å. The backbone amide proton of C185 (adjacent A186) does not interact with the primary coordination sphere of the active site and maintains a distance of 5.50 ± 0.15 Å from the apical oxo ligand throughout the simulations.

Water Transit into the Active Site. As many as 6–7 waters are observed within the combined primary coordination sphere and secondary solvation shell of the active site during these simulations (depicted in Figure 4A). Water molecules closer than ~ 3.5 Å from the molybdenum center exclusively occupy either of the exchangeable axial or equatorial coordination sites of the Mo^{IV} primary coordination sphere (illustrated in the inset structure of Figure 4B). The radial distribution function for the Mo atom and solvent is shown in Figure 4B, as well as an approximate representation of water positions in the active-site environment, based on observations from the collective simulations. Waters numbered 1 and 2 refer to the equatorial and axial waters from the primary coordination sphere, respectively. The implemented force field representation of the Mo^{IV} active site does not explicitly define bonds between the metal center and specific solvent molecules and therefore waters 1 and 2 are at slightly longer distances than expected. The occupancy for waters 3–7 (in the secondary solvation shell) is more variable

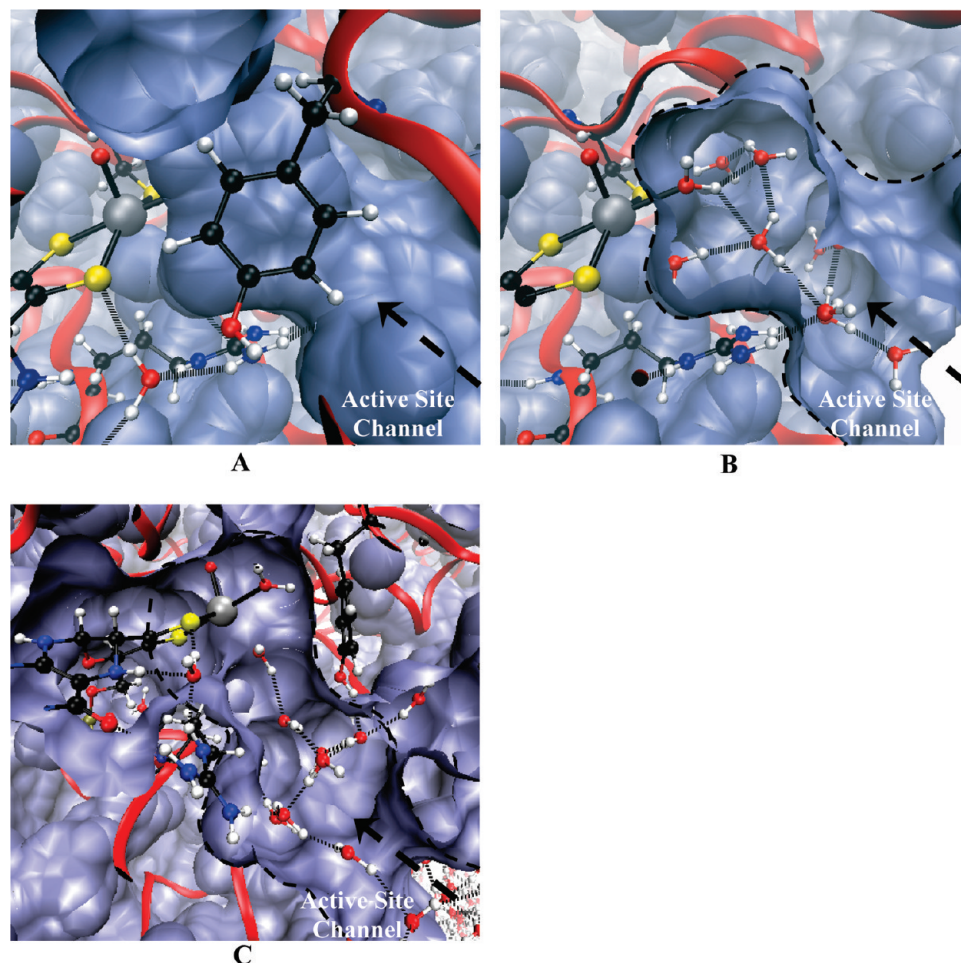


Figure 5. Cutaway view of the channel leading from the protein exterior to the active site (indicated by an arrow). Panels A and B show a cutaway of the channel when Y322 occupies a position opposite C185. Panel C shows an alternate position of Y322, where the residue occupies a approximately 90° to the position shown in panel A and is closer to C185. R138 and the active-site channel water molecules are explicitly shown in each panel.

as these molecules readily exchange, positions may be vacant, or they may alternatively be occupied by an active-site side chain.

The equatorial water molecule (H_2O 1 in Figure 4B) only exchanges in two of the simulations, while solvent in the axial position (below the equatorial plane, trans to the oxo group and denoted as H_2O 2 in Figure 4B) undergoes multiple exchanges during the course of each simulation and this position may be vacant for 10 ns or longer in some instances. As evident from the radial distribution plot in Figure 4B, both of these coordination sites are usually occupied by solvent, however waters that occupy the trans position are relatively labile while those in the equatorial position are much less so. In general, as expected, waters in the secondary solvation shell (denoted as H_2O 3–7 in Figure 4B) are not as tightly bound and exchange readily.

In these simulations, the equatorial water molecule is often partially blocked from forming numerous H-bonds due to the position and orientation of Y322 side chain (Figure 5A–C), which blocks this site for extended durations in all simulations. Occasionally, Y322 allows the equatorially bound water greater access to the active-site channel and extended H-bond networks between solvent molecules can form, extending from the active site to outside the active-site channel (Figure 5B,C). The representative cutaway views of the active-site channel in Figure 5A,C show two alternate positions of Y322, where the channel is effectively “open” and a continuous H-bond network is formed. The H-bond network residing in the channel below

Y322 in Figure 5A is shown in the cutaway view in Figure 5B. Water molecules in the axial position trans to the apical oxo ligand, however, frequently form H-bond interactions with R138 as well as with other solvent molecules within the active-site channel.

In the 1SOX crystal structure, only one oxygen atom is resolved in the equatorial position at the molybdenum center;⁹ however, its protonation state is ambiguous as individual protons are not resolved and there are likely contributions from mixed oxidation states at the molybdenum center due to photoreduction during the course of diffraction data acquisition. This O atom is from a solvent molecule in these simulations but may be either a bound H_2O or OH^- , depending on the oxidation state of the molybdenum. Analysis of high-resolution EXAFS of the Mo^{IV} form indicates the donor atom is at a distance of 2.30 Å, indicating a bound water molecule.²⁶ There are also several key residues in the vicinity of the active site which show significant stabilizing interactions with solvent molecules during their transit along the channel leading to the active site. Figure 6 summarizes the most relevant stabilizing interactions between active-site residues and primary coordination shell waters 1 and 2 from one representative simulation. In addition, interactions between active-site residues and solvent in the active-site channel range from -1 to -10 kJ mol⁻¹ for Y322, -2 to -15 kJ mol⁻¹ for W204, -10 to -20 kJ mol⁻¹ for N320, and -20 to -30 kJ mol⁻¹ for some waters which interact with R450 or W317.

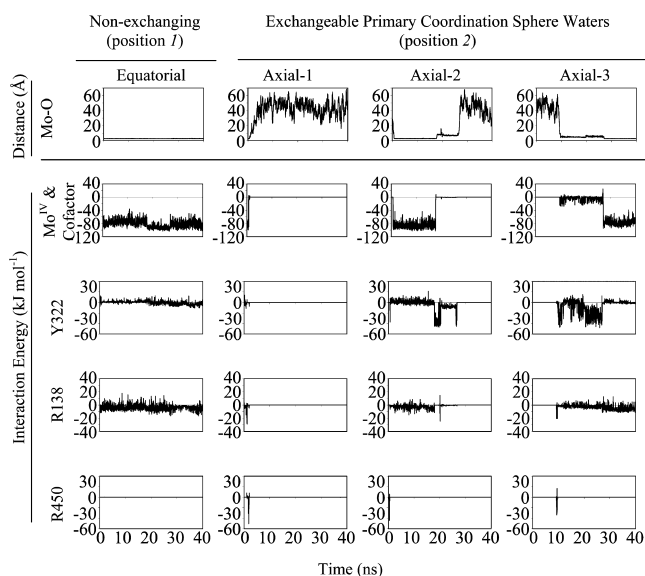


Figure 6. Representative data from an individual simulation, demonstrating the mobility of specific solvent molecules and their interactions in the primary coordination sphere of the Mo-containing active site. The equatorial water molecule (water 1) does not exchange in this simulation, while three separate water molecules exchange in the axial position (water 2) and are followed during the course of the particular simulation (designated Axial-1, -2, and -3).

As indicated earlier, in only two simulations was an equatorial water molecule observed to exit the Mo^{IV} coordination sphere. In each instance, the hydroxyl O atom of Y322 interacts with the Mo^{IV} center for a brief period before another water molecule inserts into the binding site. No such interaction has been reported previously between molybdenum and Y322 and may be an artifact of the particular force field representation of the molybdenum active site that has been used. In all other simulations, the equatorial water molecule is not significantly perturbed for the duration of the simulation (see, for example, the $\text{Mo}-\text{O}_{\text{water}}$ distance plot for H_2O 1 in Figure 6).

The axial coordination (position 2 in Figure 4B) is often occupied by an exchangeable water, and waters that are H-bonded to either the C185 thiolate (position 3 in Figure 4 B) or H-bonded between the equatorial and axial waters (H_2O 4) are usually present in these positions, although waters 3 and 4 are highly labile). Waters H-bonded to the pterin thiolate closest to the active-site channel (H_2O 5) or between the equatorial water and the water H-bonded to the C185 thiolate (H_2O 6) are also highly labile, and solvent occupancy in these positions is infrequent. Occasionally, solvent molecules H-bond to the apical oxo ligand at the molybdenum center; however, this site (H_2O 7) is the least frequently occupied of those considered due to the presence of alternate H-bond partners for the oxo ligand from A186 and A297, described above.

Figure 6 shows a comparison of equatorial (H_2O 1 in Figure 4B) and axial (H_2O 2) solvent molecules during the course of one specific 40 ns simulation. The upper panel in Figure 6 is the $\text{Mo}-\text{O}_{\text{water}}$ distances over the course of the simulation. The equatorial water does not exit the primary coordination sphere in this simulation. In contrast to the equatorial position, however, three different waters are observed to exchange in the axial position, where the position 2 $\text{Mo}-\text{O}_{\text{water}}$ distances clearly demonstrate water exchange from bulk solvent into the active-site channel and into the primary coordination sphere of Mo, and vice versa. The interaction energies for each of these waters with the Mo^{IV} active site, as well as selected residues (R138, Y322, and R450) are also shown in Figure 6. Y322 strongly

interacts with axial solvent during exchange, but its interaction is minimal once solvent occupies the apical position. R138 interacts to a minimal extent with solvent in positions 1 or 2, while R450, on the other hand, interacts strongly with solvent during capture and entry into the active-site channel. Examination of solvent interactions with other residues in the active site reveals that the residues either interact negligibly, or randomly, with solvent entering the channel or the active site and are therefore not shown.

DFT Calculations on Stabilities of Primary Coordination Sphere Waters. To evaluate the strength of water binding at the Mo^{IV} center in a more rigorous fashion, a model of the active site was constructed with and without the primary coordination sphere water molecules and geometry optimized using DFT; a representative structure is shown in Figure 4C with an equatorial water bound. In the MD simulations, the waters take up positions typical of a pseudo-octahedral coordination environment, despite the force field maintaining the explicit Mo^{IV} ligand environment in a square pyramidal geometry. Both DFT structures form square pyramidal geometries, where the apical water only weakly interacts through H-bonding with the molybdenum S-donor ligands, as opposed to coordinating to the molybdenum center.

Analysis of the interaction energy from simulations gives the magnitude of interaction between waters in positions 1 and 2 and Mo^{IV} active site as -81.3 ± 8.5 and -78.6 ± 9.0 kJ mol^{-1} , respectively (shown in Figure 6). Free energy calculations of H_2O binding in DFT-optimized structures of the Mo^{IV} active site give ΔG for coordination of the equatorial water as -72.2 kJ mol^{-1} (using a reduced dielectric constant, ϵ , of 4 for the interior of the enzyme). Coordination of the second water molecule to position 2, however, is significantly weaker compared to its force field representation, where the DFT result suggests a limit of $\Delta G < 20$ kJ mol^{-1} . The bond energy for axial water coordination to Mo^{IV} is problematic to calculate in the absence of the surrounding protein and solvent molecules due to the more favorable formation of H-bonds between water and the deprotonated S atoms which comprise the coordination sphere. In this instance, a more favorable structure with the water H-bonded to the coordinating S^- atoms (one from the dithiolene and the other from the methyl thiolate) is used as a lower limit for stabilization of the water molecule (20 kJ mol^{-1}).

As noted earlier, in all simulations the waters in the primary coordination sphere are observed to exchange; however, the equatorial water molecule is the least labile. This same O atom is resolved in the equatorial position in the ISOX crystal structure⁹ and is expected to be tightly bound based on the DFT-calculated free energy.

Discussion

Through parametrization of the molybdenum active site, the current results have demonstrated the feasibility of simulating molybdenum-containing enzyme dynamics without requiring computationally costly all-electron representations of the metal-containing cofactors. Further parametrization of the Mo^{V} and Mo^{VI} oxidation states of the active site, as well as parametrization of the Fe^{II} and Fe^{III} forms of the heme prosthetic group for the OPLS force field is ongoing.

The current results show that the heme domain is highly mobile, with ≥ 30 Å range of separation (27–57 Å) measured between the active-site Mo atom to the heme domain Fe. Such motions are expected to be important for IET from the molybdenum active site during catalytic turn over; however, significantly shorter separations than those observed here (in

the 15 Å range) are expected to be requisite for efficient IET. As discussed above, the simulations reported herein consider the half-dimer only in order to make the calculations computationally tractable. We note that simulations of the full dimer represent a formidable challenge with available computational hardware and innovative solutions such as the use of GPU-based computer clusters may be needed.⁴⁵ Intersubunit electron transfer is a possibility with the full sulfite oxidase dimer which we now address. The monomer simulations reported here do not show large changes in protein folding in the region of the interface between the two monomers. In the ISOX crystal structure the Mo–Mo separation is approximately 40 Å, and unless large conformational changes along the interface between the two monomers occur in solution (which seems unlikely), we predict that this distance will not change. The separation of 40 Å is sufficiently large that it precludes significant electron transfer between the two molybdenum atoms of the two subunits. The crystallographically observed separation between the molybdenum site of one monomer and the heme of the other monomer in the dimer is approximately 50 Å, which, similarly to the two molybdenum atoms, is large enough to preclude intersubunit electron transfer. Assuming that the interface between the two monomers forming the dimer is related to that observed by crystallography, the closest approach between molybdenum and heme is predicted to be even greater than that of the crystal structure at approximately 64 Å. Thus, the distances between the redox active sites in the two monomers are sufficiently large that intersubunit electron transfer can be excluded unless dynamic interaction between the subunits causes large scale structural changes. We plan to address this in future simulations of the complete SO dimer structure.

Feng et al. have proposed that close approach of the heme- and active-site-containing domains is likely to be mediated by electrostatic interactions via the anionic heme site and the cationic opening of the active-site channel.¹² Although the heme domain is highly mobile in these simulations, the reason such a significantly close approach of the domains is not observed may be due to several factors. Each of the eight simulations ran for a total time of 30–45 ns, beginning from an energy-minimized structure based on the crystal structure ISOX. The duration of the individual simulations may not be long enough to allow the two domains of the protein to fold into a more compact conformation conducive to IET. A second important factor is related to the simulation box size and the use of periodic boundary conditions. Snapshots from the simulations reveal that, occasionally, when the molecule is maximally extended, the surface atoms in part of the heme domain can “see” the reflected periodic image of several atoms in the C-terminal domain (such as the side chain of cationic His227), as the separation between these atoms falls just below the 10 Å cutoff for calculating nonbonded interactions. This type of problem is known to bias conformational sampling and would increase the population of the fully extended molecule over more compact forms. Finally, it may be that the process of crystallization favors hydrophobic interactions between the two domains as opposed to electrostatic interactions which would favor IET. In this case, the initial conformation taken from the crystal structure may be far from the hypothesized compact structure.

Analysis of dynamics at the molybdenum active site has demonstrated the conformational flexibility for a key residue, Y322, which appears to gate solvent access to and from the primary and secondary coordination sphere of the active site. R138 is also vital for catalytic efficiency, but this residue appears to interact minimally (considering interaction energy)

with solvent in the vicinity of the active site. This is perhaps not surprising, as the cationic R138 side chain is proposed to be involved in the capture of the anionic substrate (SO_3^{2-}) and would interact more strongly with substrate than water due to charge–charge interaction. In these simulations, R138 maintains its close proximity to the partially anionic pterin moiety.

The reactive equatorial coordination site at the molybdenum center was not explicitly coordinated to any specific ligand (indicated in Figure 1C). Although the description of ligand coordination to a metal center is expected to be inadequate using a mechanical force field representation and without an explicit metal–solvent bond force constant, geometry, or charge parameters, the as-designed model affords a tractable first approach for of studying the dynamics of ligand exchange (in this case solvent) within the active-site environment.

Dynamic motion of waters within the active-site channel as well as exchange of waters within the primary and secondary coordination sphere of the active site shed light on the accessibility of the active site and the key residues involved in transport of water molecules into the active site. Individual waters can be transferred from bulk solution to the active site, and vice versa, in ~ 1.5 ns, or can reside in the channel for 8 ns or longer. The positions of waters in the active site, such as in Figure 5B, may also indicate likely substrate positions; however, further simulations on the dioxo Mo^{VI} active site are required to fully assess this.

Tracking the energetics of specific waters as they move into and out of the active-site channel reveals key residues involved during the capture and release of solvent. The Y322 and R450 residues have been proposed to be important in substrate capture and catalytic activity;^{9,17,20} results herein confirm that these residues do play a role in molecular transport into the active site. The observed interactions are important because the stabilizing effect of the polar and positively charged residues on water molecules along the channel will be much greater with an anionic substrate or product molecules than for water. The lack of direct or specific interactions between R138 and solvent in the secondary solvation shell indicates a more specialized function for this residue, likely requiring the presence of substrate (SO_3^{2-}) or product (SO_4^{2-}) for its observation. A role for R138 in orienting groups for IET has also been proposed previously.⁴⁶

In these simulations, the primary coordination sphere equatorial water molecule is strongly bound (-81 kJ mol^{-1}) and DFT gives this interaction energy as -72 kJ mol^{-1} . The axial water was not expected to be tightly bound to the molybdenum center due to the lack of experimental evidence; however, in MD simulations this water was bound by -79 kJ mol^{-1} , while DFT indicates a -20 kJ mol^{-1} interaction limit.

In conclusion, we have shown that the domains of sulfite oxidase are highly mobile, and that the previously postulated domain motion is reasonable, and probably will occur in solution. Finally, our calculations on the active-site dynamics provide important information on possible roles of different active-site amino acid residues. Further molecular dynamics simulations of the full-length SO dimer employing fully parametrized heme groups and alternate oxidation states of both molybdenum and heme active sites are presently ongoing.

Acknowledgment. Support from the Saskatchewan Health Research Foundation and a Canada Research Chair award (to G.N.G.) and the Saskatchewan Health Research Foundation are

acknowledged. Work at the University of Saskatchewan was supported by the Saskatchewan Health Research Foundation, the Natural Sciences and Engineering Research Council Canada, the Canadian Institutes of Health Research, and by a Canada Research Chair award. This research has been enabled by the use of WestGrid computing resources, which are funded in part by the Canada Foundation for Innovation, Alberta Innovation and Science, BC Advanced Education, and the participating research institutions. WestGrid equipment is provided by IBM, Hewlett-Packard, and SGI.

Supporting Information Available: DFT-optimized structures for the Mo- and Fe-containing coordination sites. Motions from normal mode analysis. This material is available free of charge via the Internet at <http://pubs.acs.org>.

References and Notes

- (1) McLeod, R. M.; Farkas, W.; Fridovitch, I.; Handler, P. Purification and properties of hepatic sulfite oxidase. *J. Biol. Chem.* **1961**, *236*, 1841–1852.
- (2) Rees, D. C.; Tezcan, A.; Hayes, C. A.; Walton, M. Y.; Andrade, S.; Einsle, O.; Howard, J. B. Structural basis of biological nitrogen fixation. *Philos. Trans. R. Soc. London, Ser. A* **2005**, *263*, 971–984.
- (3) Rajagopalan, K. V. Novel aspects of the biochemistry of the molybdenum cofactor. *Adv. Enzymol. Relat. Areas Mol. Biol.* **1991**, *64*, 215–290.
- (4) Rajagopalan, K. V.; Johnson, J. L. The pterin molybdenum cofactors. *J. Biol. Chem.* **1992**, *267*, 10199–10202.
- (5) Eilers, T.; Schwarz, G.; Brinkmann, H.; Witt, C.; Richter, T.; Nieder, J.; Koch, B.; Hille, R.; Hensch, R.; Mendel, R. R. Identification and biochemical characterization of *Arabidopsis thaliana* sulfite oxidase. A new player in plant sulfur metabolism. *J. Biol. Chem.* **2001**, *276*, 46989–46994.
- (6) Kappler, U.; Bennett, B.; Rethmeier, J.; Schwarz, G.; Deutzmann, R.; McEwan, A. G.; Dahl, C. Sulfite:cytochrome c oxidoreductase from *Thiobacillus novellus*: purification, characterization, and molecular biology of a heterodimeric member of the sulfite oxidase family. *J. Biol. Chem.* **2000**, *275*, 13202–13212.
- (7) Seidahmed, M. Z.; Alyamani, E. A.; Rashed, M. S.; Saadallah, A. A.; Abdelbasit, O. B.; Saheed, M. M.; Rasheed, A.; Hamid, F. A.; Sabry, M. A. Total truncation of the molybdopterin/dimerization domains of SUOX protein in an Arab family with isolated sulfite oxidase deficiency. *Am. J. Med. Genet. Part A* **2005**, *136A*, 205–209.
- (8) Steinberg, K. K.; Relling, M. V.; Gallagher, M. L.; Greene, C. N.; Rubin, C. S.; French, D.; Holmes, A. K.; Carroll, W. L.; Koontz, D. A.; Sampson, E. J.; Satten, G. A. Genetic studies of a cluster of acute lymphoblastic leukemia cases in Churchill County, Nevada. *Environ. Health Perspect.* **2007**, *115*, 158–164.
- (9) Kisker, C.; Schindelin, H.; Pacheco, A.; Wehbi, W. A.; Garrett, R. M.; Rajagopalan, K. V.; Enemark, J. H.; Rees, D. C. Molecular basis of sulfite oxidase deficiency from the structure of sulfite oxidase. *Cell* **1997**, *91*, 973–983.
- (10) Enroth, C.; Eger, B. T.; Okamoto, K.; Nishino, T.; Nishino, T.; Pai, E. F. Crystal structures of bovine milk xanthine dehydrogenase and xanthine oxidase: Structure-based mechanism of conversion. *Proc. Natl. Acad. Sci. U.S.A.* **2000**, *97*, 10723–10728.
- (11) Rebelo, J.; Macieira, S.; Dias, J. M.; Huber, R.; Ascenso, C. S.; Rusnak, F.; Moura, J. J.; Moura, I.; Romao, M. J. Gene sequence and crystal structure of the aldehyde oxidoreductase from *Desulfovibrio desulfuricans* ATCC 27774. *J. Mol. Biol.* **2000**, *297*, 135–146.
- (12) Feng, C.; Kedia, R. V.; Hazzard, J. T.; Hurley, J. K.; Tollin, G.; Enemark, J. H. Effect of Solution Viscosity on Intramolecular Electron Transfer in Sulfite Oxidase. *Biochemistry* **2002**, *41*, 5816–5821.
- (13) Kawatsu, T.; Beratan, D. N. Electron transfer between cofactors in protein domains linked by a flexible tether. *Chem. Phys.* **2006**, *326*, 259–269.
- (14) Johnson, J. L.; Rajagopalan, K. V. Tryptic cleavage of rat liver sulfite oxidase. Isolation and characterization of molybdenum and heme domains. *J. Biol. Chem.* **1977**, *252*, 2017–2025.
- (15) Feng, C.; Wilson, H. L.; Hurley, J. K.; Hazzard, J. T.; Tollin, G.; Rajagopalan, K. V.; Enemark, J. H. Essential role of conserved arginine 160 in intramolecular electron transfer in human sulfite oxidase. *Biochemistry* **2003**, *42*, 12235–12242.
- (16) Doonan, C. J.; Wilson, H. L.; Rajagopalan, K. V.; Garrett, R. M.; Bennett, B.; Prince, R. C.; George, G. N. Modified active site coordination in a clinical mutant of sulfite oxidase. *J. Am. Chem. Soc.* **2007**, *129*, 9421–9428.
- (17) Wilson, H. L.; Rajagopalan, K. V. The role of tyrosine 343 in substrate binding and catalysis by human sulfite oxidase. *J. Biol. Chem.* **2004**, *279*, 15105–15113.
- (18) Lee, H. F.; Mak, B. S. C.; Chi, C. S.; Tsai, C. R.; Chen, C. H.; Shu, S. G. A novel mutation in neonatal isolated sulfite oxidase deficiency. *Neuropediatrics* **2002**, *33*, 174–179.
- (19) Pacheco, A.; Hazzard, J. T.; Tollin, G.; Enemark, J. H. The pH dependence of intramolecular electron transfer rates in sulfite oxidase at high and low anion concentrations. *J. Biol. Inorg. Chem.* **1999**, *4*, 390–401.
- (20) Feng, C.; Wilson, H. L.; Hurley, J. K.; Hazzard, J. T.; Tollin, G.; Rajagopalan, K. V.; Enemark, J. H. Role of conserved tyrosine 343 in intramolecular electron transfer in human sulfite oxidase. *J. Biol. Chem.* **2003**, *278*, 2913–2920.
- (21) Becke, A. D. Density-functional thermochemistry. III. The role of exact exchange. *J. Chem. Phys.* **1993**, *98*, 5648–5652.
- (22) Frisch, M. J.; Trucks, G. W.; Schlegel, H. B.; Scuseria, G. E.; Robb, M. A.; Cheeseman, J. R.; Montgomery, Jr., J. A.; Vreven, T.; Kudin, K. N.; Burant, J. C.; Millam, J. M.; Iyengar, S. S.; Tomasi, J.; Barone, V.; Mennucci, B.; Cossi, M.; Scalmani, G.; Rega, N.; Petersson, G. A.; Nakatsuji, H.; Hada, M.; Ehara, M.; Toyota, K.; Fukuda, R.; Hasegawa, J.; Ishida, M.; Nakajima, T.; Honda, Y.; Kitao, O.; Nakai, H.; Klene, M.; Li, X.; Knox, J. E.; Hratchian, H. P.; Cross, J. B.; Bakken, V.; Adamo, C.; Jaramillo, J.; Gomperts, R.; Stratmann, R. E.; Yazyev, O.; Austin, A. J.; Cammi, R.; Pomelli, C.; Ochterski, J. W.; Ayala, P. Y.; Morokuma, K.; Voth, G. A.; Salvador, P.; Dannenberg, J. J.; Zakrzewski, V. G.; Dapprich, S.; Daniels, A. D.; Strain, M. C.; Farkas, O.; Malick, D. K.; Rabuck, A. D.; Raghavachari, K.; Foresman, J. B.; Ortiz, J. V.; Cui, Q.; Baboul, A. G.; Clifford, S.; Cioslowski, J.; Stefanov, B. B.; Liu, G.; Liashenko, A.; Piskorz, P.; Komaromi, I.; Martin, R. L.; Fox, D. J.; Keith, T.; Al-Laham, M. A.; Peng, C. Y.; Nanayakkara, A.; Challacombe, M.; Gill, P. M. W.; Johnson, B.; Chen, W.; Wong, M. W.; Gonzalez, C.; Pople, J. A. *Gaussian 03, Revision E.01*; Gaussian Inc.: Wallingford, CT, 2004.
- (23) Kaminski, G.; Duffy, E. M.; Matsui, T.; Jorgensen, W. L. Free energies of hydration and pure liquid properties of hydrocarbons from the OPLS all-atom model. *J. Phys. Chem.* **1994**, *98*, 13077–13082.
- (24) Jorgensen, W. L.; Maxwell, D. S.; Tirado-Rives, J. Development and testing of the OPLS all-atom force field on conformational energetics and properties of organic liquids. *J. Am. Chem. Soc.* **1996**, *118*, 11225–11236.
- (25) George, G. N.; Kipke, C. A.; Prince, R. C.; Sunde, R. A.; Enemark, J. H.; Cramer, S. P. Structure of the active site of sulfite oxidase. X-ray absorption spectroscopy of the Mo(IV), Mo(V) and Mo(VI) oxidation states. *Biochemistry* **1989**, *28*, 5075–5080.
- (26) Harris, H. H.; George, G. N.; Rajagopalan, K. V. High resolution EXAFS of the active site of sulfite oxidase: Comparison with density functional and x-ray crystallographic results. *Inorg. Chem.* **2006**, *45*, 493–495.
- (27) Carlson, H. A.; Nguyen, T. B.; Orozco, M.; Jorgensen, W. L. Accuracy of free energies of hydration for organic molecules from 6-31g*-derived partial charges. *J. Comput. Chem.* **1993**, *14*, 1240–1249.
- (28) Pushie, M. J.; Vogel, H. J. Molecular dynamics simulations of two tandem octa-repeat sites from the mammalian prion protein in its metal free and fully copper-bound states. *Biophys. J.* **2007**, *93*, 3762–3774.
- (29) Pushie, M. J.; Vogel, H. J. Modeling by assembly and molecular dynamics simulations of the low Cu²⁺ occupancy form of the mammalian prion protein octarepeat region: gaining insight into Cu²⁺-mediated beta-cleavage. *Biophys. J.* **2008**, *95*, 5084–5091.
- (30) Brunier, T. M.; Drew, M. G. B.; Mitchell, P. C. H. Molecular mechanics study of the interaction of thiophene with a molybdenum disulfide catalyst. *J. Chem. Soc., Faraday Trans.* **1992**, *88*, 3225–3232.
- (31) Berendsen, H. J. C.; van der Spoel, D.; van Drunen, R. GROMACS: A message-passing parallel molecular dynamics implementation. *Comput. Phys. Commun.* **1995**, *91*, 43–56.
- (32) Lindahl, E.; Hess, B.; van der Spoel, D. GROMACS 3.0: A package for molecular simulation and trajectory analysis. *J. Mol. Model.* **2001**, *7*, 306–317.
- (33) Berendsen, H. J. C.; Postma, J. P. M.; DiNola, A.; Haak, J. R. Molecular dynamics with coupling to an external bath. *J. Chem. Phys.* **1984**, *81*, 3684–3690.
- (34) Essman, U.; Perera, L.; Berkowitz, M. L.; Darden, T.; Lee, H.; Pedersen, L. G. A smooth particle mesh Ewald method. *J. Chem. Phys.* **1995**, *103*, 8577–8592.
- (35) Hess, B.; Bekker, H.; Berendsen, H. J. C.; Fraaije, J. G. E. M. LINCS: A linear constraint solver for molecular simulations. *J. Comput. Chem.* **1997**, *18*, 1463–1472.
- (36) Berendsen, H. J. C.; Postma, J. P. M.; van Gunsteren, W. F.; Hermans, J. In *Intermolecular Forces*; Pullman, B., Ed.; Reidel: Dordrecht, The Netherlands, 1981; pp 331–342.

- (37) Miyamoto, S.; Kollman, P. A. Settle: An analytical version of the SHAKE and RATTLE algorithm for rigid water models. *J. Comput. Chem.* **1992**, *13*, 952–962.
- (38) Feenstra, K. A.; Hess, B.; Berendsen, H. J. C. Improving efficiency of large time-scale molecular dynamics simulations of hydrogen-rich systems. *J. Comput. Chem.* **1999**, *20*, 786–798.
- (39) Aliste, M. P.; Tieleman, D. P. Computer simulation of partitioning of ten pentapeptides Ace-WLXLL at the cyclohexane/water and phospholipid/water interfaces. *BMC Biochem.* **2005**, *6*, 30.
- (40) Chan, D. I.; Stockner, T.; Tieleman, D. P.; Vogel, H. J. Molecular Dynamics Simulations of the Apo-, Holo-, and Acyl-forms of Escherichia coli Acyl Carrier Protein. *J. Biol. Chem.* **2008**, *283*, 33620–33629.
- (41) van der Spoel, D.; Lindahl, E.; Hess, B.; van Buuren, A. R.; Apol, E.; Meulenhoff, P. J.; Tieleman, D. P.; Sijbers, A. L. T. M.; Feenstra, K. A.; van Drunen, R.; Berendsen, H. J. C. Gromacs User Manual 3.3, www.gromacs.org, 2005.
- (42) <http://lorentz.immstr.pasteur.fr/nomad-ref.php>.

- (43) Tirion, M. M. Large amplitude elastic motions in proteins from a single-parameter, atomic analysis. *Phys. Rev. Lett.* **1996**, *77*, 1905–1908.
- (44) Bahar, I.; Atilgan, A. R.; Erman, B. Direct evaluation of thermal fluctuations in proteins using a single parameter harmonic potential. *Folding Des.* **1997**, *1*, 357–370.
- (45) Friedrichs, M. S.; Eastman, P.; Vaidyanathan, V.; Houston, M.; Legrand, S.; Beberg, A. L.; Ensign, D. L.; Bruns, C. M.; Pande, V. S. Accelerating molecular dynamic simulation on graphics processing units. *J. Comput. Chem.* **2009**, *30*, 864–872.
- (46) Emesh, S.; Rapson, T. D.; Rajapakshe, A.; Kappler, U.; Bernhardt, P. V.; Tollin, G.; Enemark, J. H. Intramolecular Electron Transfer in Sulfite-Oxidizing Enzymes: Elucidating the Role of a Conserved Active Site Arginine. *Biochemistry* **2009**, *48*, 2156–2163.

JP908731F